1992-12

Solid state x-ray detector calibration techniques and LINAC beam intensity measurements

Fasanello, Thomas J.

REPORT DOCUMENTATION PAGE

1a. REPORT SECURITY CLASSIFICATION Unclassified	1b. RESTRICTIVE MARKINGS
2a. SECURITY CLASSIFICATION AUTHORITY	3. DISTRIBUTION/AVAILABILITY OF REPORT Approved for public release; distribution is unlimited.
2b. DECLASSIFICATION/DOWNGRADING SCHEDULE	
4. PERFORMING ORGANIZATION REPORT NUMBER(S)	5. MONITORING ORGANIZATION REPORT NUMBER(S)
6a. NAME OF PERFORMING ORGANIZATION Naval Postgraduate School 6b. OFFICE SYMBOL (*If applicable*) 39	7a. NAME OF MONITORING ORGANIZATION Naval Postgraduate School
6c. ADDRESS (*City, State, and ZIP Code*) Monterey, CA 93943-5000	7b. ADDRESS (*City, State, and ZIP Code*) Monterey, CA 93943-5000
8a. NAME OF FUNDING/SPONSORING ORGANIZATION 8b. OFFICE SYMBOL (*If applicable*)	9. PROCUREMENT INSTRUMENT IDENTIFICATION NUMBER
8c. ADDRESS (*City, State, and ZIP Code*)	10. SOURCE OF FUNDING NUMBERS Program Element No / Project No / Task No / Work Unit Accession Number

11. TITLE (*Include Security Classification*)
SOLID STATE X-RAY DETECTOR CALIBRATION TECHNIQUES AND LINAC BEAM INTENSITY MEASUREMENTS

12. PERSONAL AUTHOR(S) Fasanello, Thomas J.

13a. TYPE OF REPORT	13b. TIME COVERED	14. DATE OF REPORT (*year, month, day*)	15. PAGE COUNT
Master's Thesis	From To	December 1992	59

16. SUPPLEMENTARY NOTATION
The views expressed in this thesis are those of the author and do not reflect the official policy or position of the Department of Defense or the U.S. Government.

17. COSATI CODES			18. SUBJECT TERMS (*continue on reverse if necessary and identify by block number*)
FIELD	GROUP	SUBGROUP	Si(Li) detector characteristics, energy calibration, electron beam intensity.

19. ABSTRACT (*continue on reverse if necessary and identify by block number*)

X-ray fluorescence from thin foils inserted into the NPS linac have been used to measure the the integrated electron beam current only. The measured x-ray flux and the known inner shell ionization cross sections are used to obtain measurements of dark currents of the order of ten to the minus fourteenth amperes. The same arrangement allows continuous, in-situ energy calibration of our Si(Li) detector in the electromagnetic noise enviroment of the linac. This technique was originally developed to perform absolute production efficiency measurements of parametric x-ray generation in the 5-50 KeV range.

20. DISTRIBUTION/AVAILABILITY OF ABSTRACT	21. ABSTRACT SECURITY CLASSIFICATION	
☒ UNCLASSIFIED/UNLIMITED ☐ SAME AS REPORT ☐ DTIC USERS	Unclassified	
22a. NAME OF RESPONSIBLE INDIVIDUAL Xavier K. Maruyama	22b. TELEPHONE (*Include Area code*) (408) 646-2431	22c. OFFICE SYMBOL PH/Mx

Approved for public release; distribution is unlimited.

Solid State X-ray Detector Calibration Techniques and LINAC Beam Intensity Measurements

by

Thomas J. Fasanello Jr.
Lieutenant , United States Navy
B.S., U.S. Naval Academy, 1985

Submitted in partial fulfillment
of the requirements for the degree of

MASTER OF SCIENCE IN PHYSICS

from the

NAVAL POSTGRADUATE SCHOOL
December 1992

ABSTRACT

X-ray fluorescence from thin foils inserted into the NPS linac has been used to measure the integrated electron beam intensity when the accelerator is operating with dark current only. The measured x-ray flux and the known inner shell ionization cross sections are used to obtain measurements of dark currents of the order of 10^{-14} amperes. The same arrangement allows continuous, in-situ energy calibration of our Si(Li) detector in the electromagnetic noise environment of the linac. This technique was originally developed to perform absolute production efficiency measurements of parametric x-ray generation in the 5-50 KeV range.

TABLE OF CONTENTS

ACKNOWLEDGEMENTS

My sincere thanks to Professor X. K. Maruyama for his support, guidance and willingness to explain things more than once. His tenacity and humor have made this endeavor a worthwhile and rewarding experience.

Thanks to Dr. Scofield and Dr. Seltzer without whose data much of this project would not be possible. My appreciation also to Dr. Mel Piestrup for his critique of this thesis.

Also thanks to Mr. Don Snyder and Mr. Harold Reitdyk of the NPS Linear Accelerator. Without their dedication and expertise the ability to collect meaningful data would be impossible.

I. INTRODUCTION

A. BACKGROUND

At the Naval Postgraduate School we have a program to measure the characteristics of parametric x-ray radiation. Parametric x-ray radiation, PXR, can be used to create a tuneable x-ray source. PXR is generated by placing natural or synthetic crystals, or multilayer structures into the path of a relativistic electron beam. The virtual photons associated with the coulomb fields of incoming electrons are Bragg reflected by the periodic crystal lattice and real x-rays appear at the Bragg angle. The production process is analagous to x-ray diffraction by crystals, except that the x-ray beam incident at the Bragg angle is replaced by a relativistic electron beam [Ref. 1].

Figure 1 shows the target chamber configuration and geometry between the crystal, electron beam and detector for the generation of parametric x-ray radiation.

The x-rays were observed with a solid state, Si(Li) detector. The detector is highly efficient in the energy range required for this experiment, from 3 to 5 KeV up to approximately 35 KeV.

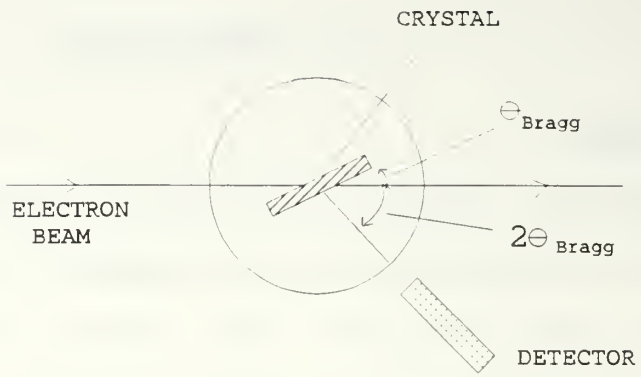

Figure 1. PXR target chamber configuration.

B. ENERGY CALIBRATION

Parametric x-ray is generated and measured during the macropulse structure of the electron linear accelerator. The environment in which the x-rays are generated has high electromagnetic noise due to the linear accelerator, principally due to the RF klystrons. This creates several problems, most signifigant of which is an accurate method of calibrating the energy scale to which the incoming PXR can be compared.

The x-rays incident upon the detector create a voltage signal proportional to the energy which is then sent to a pulse height analyzer. Each voltage signal is assigned a channel number corresponding to the magnitude of the voltage. A sample of the PXR data collected is shown in Figure 2.

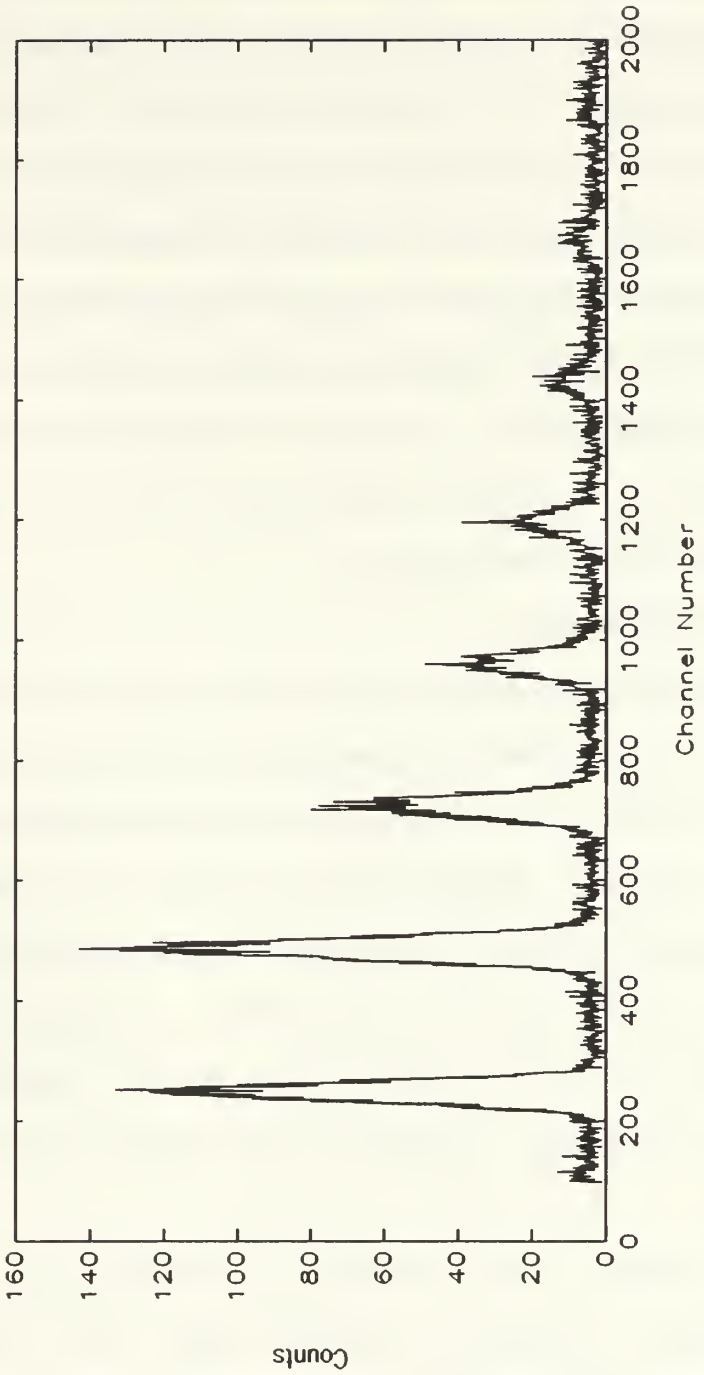

Figure 2. PXR spectrum using carbon graphite. The number of counts in each peak is plotted versus the channel number the energy was collected at [Ref.2].

A method to precisely calibrate the energy scale such that each channel number is correlated to a specific energy needed to be developed. If a target is placed in the path of the electron beam de-excitation photon emissions from the K-edge of atoms excited by the beam can be observed. These emissions are of known energies and will allow for in-situ energy calibration in the electromagnetic noise enviroment of the linear accelerator. We have developed an x-ray energy calibration technique applicable to the measurement of parametric x-ray radiation.

C. BEAM INTENSITY

When PXR is measured, the total number of x-rays produced at a particular energy is recorded. This data yields the total number of photons created without information as to the flux of the incident electrons. In order to compare the PXR spectrum with theory, the number of photons produced for every electron incident upon the crystal, or absolute flux, must be determined. It is therefore necessary to determine the total number of electrons incident on the crystal for a given set of PXR data.

PXR rocking data involves rotating the crystal through small angles about the Bragg angle and comparing x-ray intensity measurements at the different angles. Normalization

of the rocking data also requires the total number of electrons incident upon the crystal during the data collection time to be known.

It is therefore necessary to determine the integrated electron fluence on the PXR crystal target. We have developed a technique to measure the incident electron flux from the x-ray fluorescence which is also used for energy calibration.

II. Si(Li) DETECTOR CHARACTERISTICS

The detector used in the measurement of parametric x-rays is an Si(Li) solid state semiconductor detector. Advantages of this type of detector are the efficiency of detection in the energy range of interest and the energy resolution possible due to the large number of charge carriers produced for every pulse of incoming radiation.

A. SEMICONDUCTOR PROPERTIES

Semiconductors are materials that are crystalline in structure, most notably silicon, which form covalent bonds. At temperatures above absolute zero, some of the covalent bonds are broken allowing for free electrons, n, to conduct in the medium, leaving a hole behind in the valence band [Ref. 3]. This configuration of conduction band and valence band is shown in Figure 3.

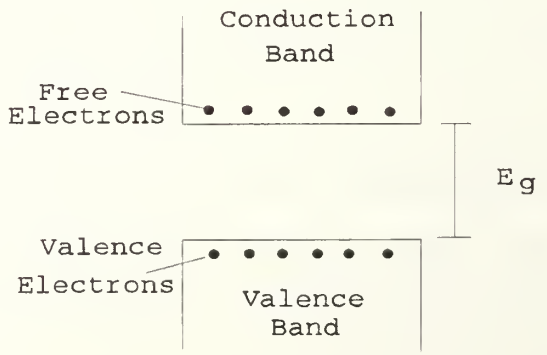

Figure 3. Relationship between conduction and valence bands in a semiconductor.

If a certain amount of impurity atoms are introduced to the silicon in which either electrons or holes are predominant, the resulting crystal is known as an extrinsic material. The impurity , or dopant, need only be introduced in small concentrations, $1:10^7$ [Ref. 4], to have the desired effect.

If the dopant added has five valence electrons, the crystal is called an n-type material. The n-type material's fifth valence electron donates excess electron carriers which are known as donor impurities. Even though the donor impurities are of such small concentrations,conductivity can be increased signifigantly, as much as 10^5 times [Ref. 4]. The net effect is that the number of free electrons available for conduction is increased.

If the silicon crystal is doped with a material having three valence electrons, a p-type material will be created. Due to the trivalent nature of the bond in the impurity, a hole exists that can be filled by an electron. The net effect of this process is that the energy level of the acceptor atoms is just above the valence band.

When the p-type and n-type materials are placed together a p-n junction is formed. Holes will attempt to diffuse to the n region thus combining with free electrons and are neutralized. The number of free electrons is thereby reduced, causing a net positive charge on the n side. The holes that

attempted to diffuse cause a net negative charge on the p side. This small region of positive and negative charges is known as the depletion region (Figure 4).

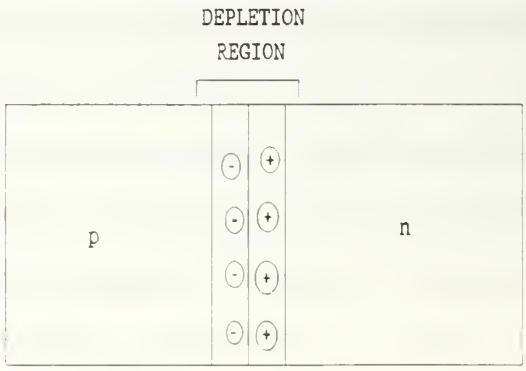

Figure 4. Semiconductor p-n junction and depletion region.

This depletion region is is referred to as the active volume of the detector.

The major limitation is the maximum depletion depth or active volume that can be achieved. Despite using materials with the highest available resistivity, with a reverse bias near the breakdown value, depletion depths beyond 2-3 mm are difficult to achieve. Much greater thicknesses are required for x-ray spectroscopy. [Ref. 5]

A process known as ion drifting is used to overcome this problem. This process involves creating a relatively thick

region of compensated material in which the number of acceptor impurities equals the number of donor impurities.

Lithium is diffused into one surface of the p-type silicon to form a p-n junction. Then lithium atoms from the n-type layer are made to drift through the silicon, taking up positions within the material to compensate for the original p-type impurities and creating an intrinsic region. The p-type region is covered by a thin gold surface barrier which is transparent to soft x-rays [Ref. 6].

When incoming x-rays are incident upon the semiconductor, electron-hole pairs are created. If an electric field is applied across the intrinsic region, electrons and positive charges will travel in opposite directions with respect to the electric field. The electric field is created by applying a bias voltage across the p-i-n junction. The charge that is created is directly proportional to the incoming radiation. The detector used for this experiment collected one charge for every 3.5 eV incident upon the detector [Ref. 6]. In our experiment for a 5 KeV photon approimately 1.43×10^3 free charges were collected. The detector configuration is shown in Figure 5.

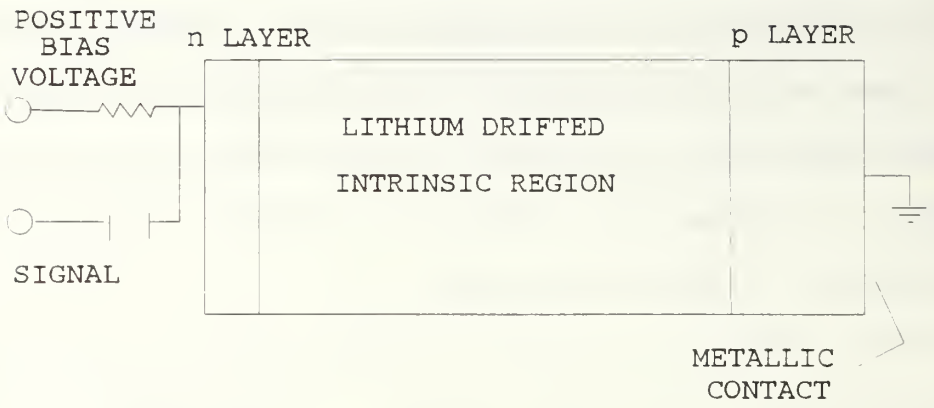

Figure 5. Configuration of p-i-n junction [Ref. 5].

B. DETECTOR CHARACTERISTICS

1. Linearity

The response of the Si(Li) detector is linear. Energy deposited on the detector in the form of x-ray radiation is proportional to the number of electron-hole pairs. The voltage signal sent to the pulse height analyzer is proportional to the number of charge carriers created from the energy deposition. The linearity property is shown in Figure 6 using the PHA spectrum obtained from the target foil of titanium, yttrium and tin.

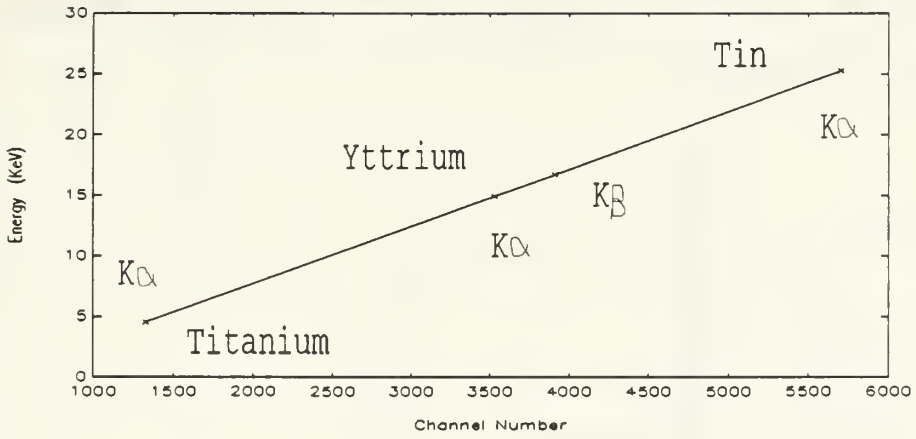

Figure 6. Linearity of x-ray energy deposited versus PHA channel number.

2. Response Function

In silicon, the photoelectric process is more probable than Compton scattering for photon energies below 55 KeV [Ref. 5]. For x-rays of very low energies, less than 5 KeV, there is a loss of efficiency in detection due to the attenuation of the photons and most photoelectric absorptions occur near the surface of the detector. The photoelectric absorption can cause a characteristic x-ray of the silicon to be produced and since the absorption is near the surface of the detector, the resulting x-ray can escape the detector. For silicon, the K_α peak occurs at 1.8 keV and the resulting full

energy peak of the incident x-ray energy will appear 1.8 KeV less then would be expected. The resulting escape peak is shown in Figure 7.

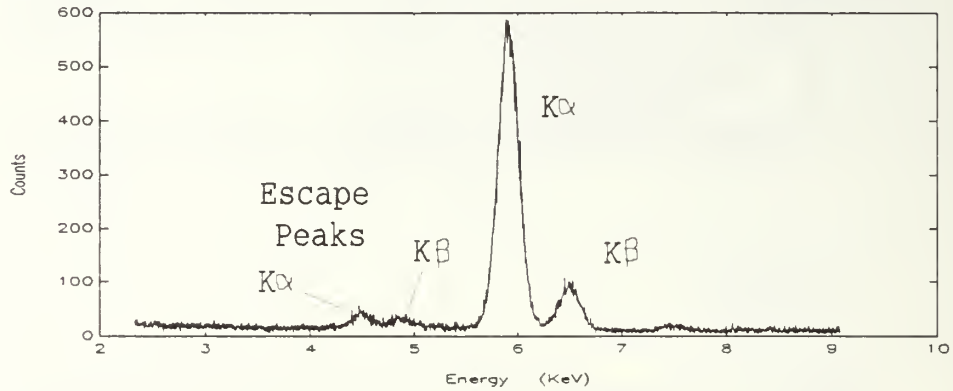

Figure 7. Peaks caused by the escape of Si x-ray from detector at low incident x-ray energies using Fe-55 source.

3. Sum-Coincidence Effects

If two x-ray events occur almost simultaneously and are incident upon the detector at nearly the same time, the total energy recorded in the pulse height spectrum will be interpreted as due to one x-ray event instead of two. The energy that is measured will be a sum of the two energies that were deposited on the detector, and the identity of the two events will be combined. This phenomenon is illustrated in Figure 8 where a yttrium foil was used as the target material.

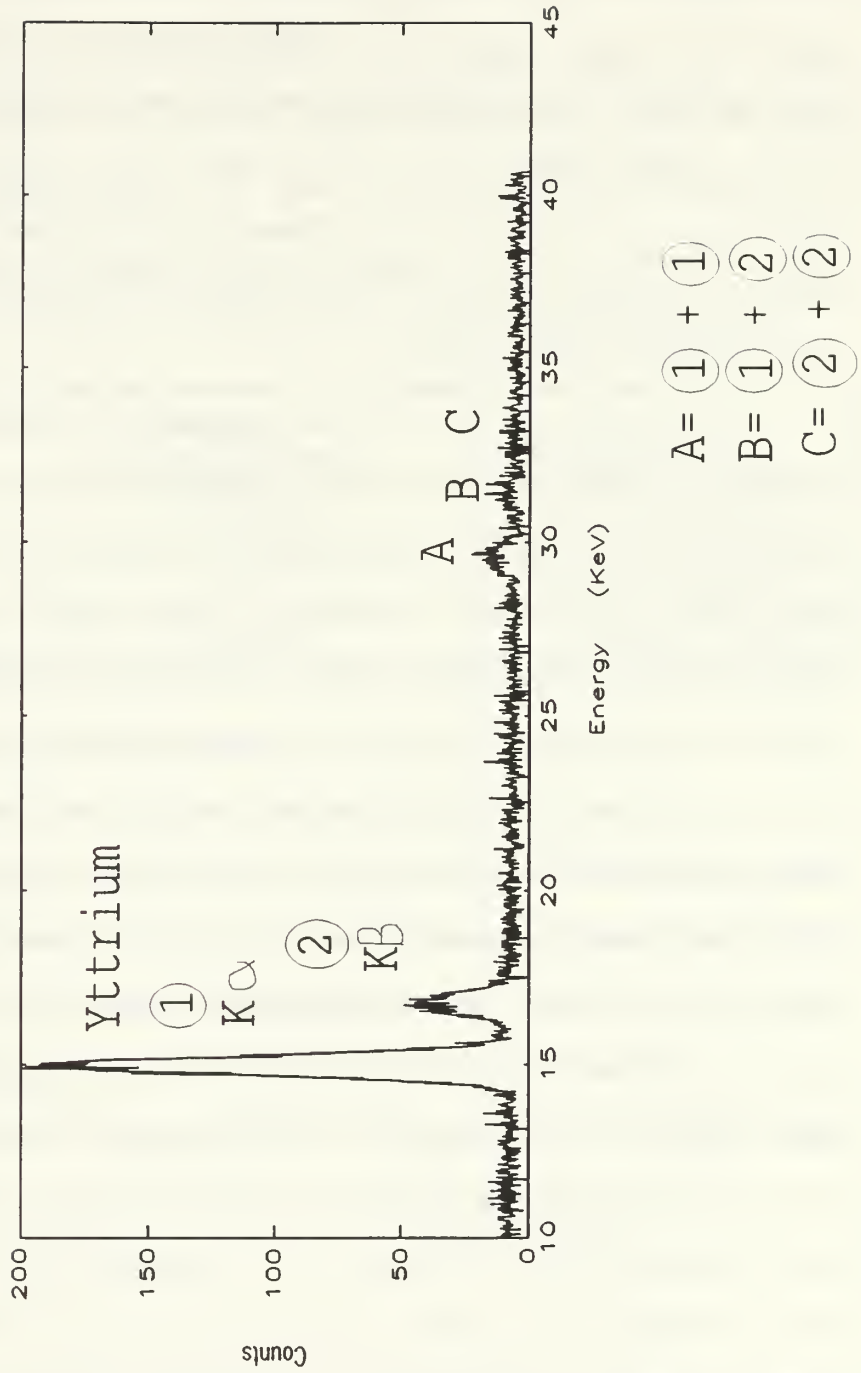

Figure 8. Illustratuion of sum-coincidence effect from characteristic peaks of Yttrium.

Although the K_α and K_β peaks are clearly evident in the spectrum, three additional energy peaks can be seen in the far end of the spectrum. These peaks are attributable to the coincident detection of two K_α deexcitations, peak A, a coincident K_β and K_α deexcitation, peak B, and two coincident K_β deexcitations, peak C.

In the analysis of parametric x-ray data it is essential that none of the information from individual peaks is lost to these sum-coincidence events. This will result in the under counting of events in some peaks, particularly the lower energy peaks, and over counting in higher energy peaks due to coincident detection events at lower energies.

To resolve this problem one of two things is possible. The probability of coincident detection can be reduced or an algorithim can be created to account for the coincident events that have occured and correct for them.

These random coincidences can be predicted using the the formula for accidental coincidence [Ref. 7]:

$$N_{random}=2N_1N_2(\rho) \qquad (1)$$

where N_1 and N_2 represent the count rates of the individual true energy events and ρ represents the resolving time of the

detector. The effective resolving time of the detector was determined to be 3 microseconds.

Using the data extracted from Figure 8 the theoretical random count rates can be compared to the count rates actually measured. This data is represented in Table I.

TABLE I. CALCULATED RANDOM COUNT RATES COMPARED TO ACTUAL COINCIDENCE PEAKS OF YTTRIUM K_α AND K_β PEAKS.

SUM COINCIDENCE PEAK	N_{random} (s^{-1}) (Theoretical)	N_{random} (s^{-1}) (Experimental)
$2K_\alpha$	$8.08 \times 10^{+3}$	$(2.89 \pm .29) \times 10^{+3}$
$K_\alpha + K_\beta$	$1.31 \times 10^{+3}$	$(2.65 \pm .22) \times 10^{+3}$
$2K_\beta$	$2.13 \times 10^{+2}$	$(4.18 \pm .21) \times 10^{+2}$

C. ELECTRONIC CONFIGURATION

For purposes of ambient noise reduction the signal from the detector is gated enroute to the pulse height analyzer. This gating process involves only processing those pulses from the detector that are centered about the signal of interest. The need to reduce ambient RF noise and maintain an energy calibration can be accomplished through use of the signal processing chain illustrated in Figure 9. The photon energy incident upon the detector is converted to a proportional voltage at the preamplifier, the signal is shaped at the amplifier and ambient RF noise is filtered out with the use of a linear gate.

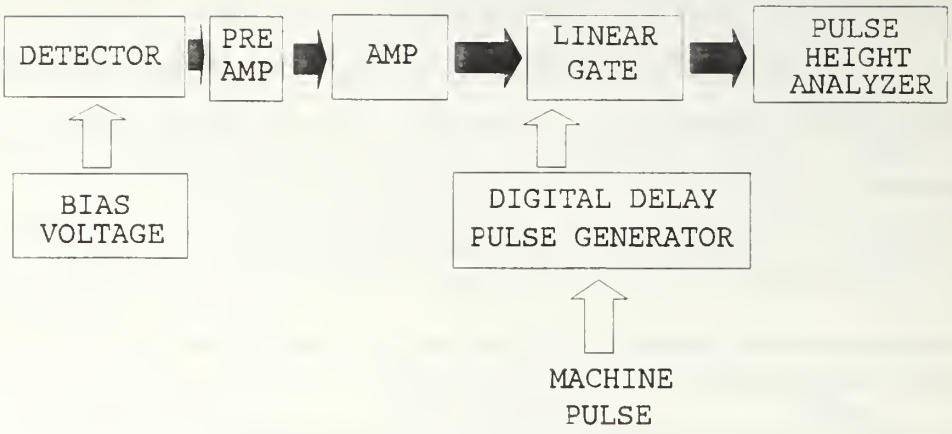

Figure 9. Schematic representation of signal flow path.

D. COMPONENT FUNCTIONS AND CHARACTERISTICS

1. Detector

X-ray energy incident upon the Si(Li) detector creates electron-hole pairs. In the presence of the electric field induced by the bias voltage these charges are collected on their respective electrodes. The amount of charge carriers produced is directly proportional to the incident energy upon the detector.

2. Preamplifier

The charge collected by the creation of electron-hole pairs within the active volume of the detector is, in general, too small for accurate energy analysis. The Canberra detector used in these experiments liberates one charge pair for every 3.5 eV incident upon the detector [Ref. 6]. The charge must be

converted to a proportional output voltage through the use of a preamplifier.

The preamplifier converts the charge from each energy absorption event to a step function pulse output whose amplitude is proportional to the total charge accumulated. The output pulse from the preamplifier decays exponentially with a time constant of 50 microseconds to allow for separation of events in high count rate situations [Ref. 2].

The detector capacitance of semiconductor detectors may change with operating parameters which gives the charge sensitive preamplifier desirable characteristics. The output voltage from the preamplifier has no dependence on the input capacitance of the detector (C_i), Figure 10 [Ref. 5].

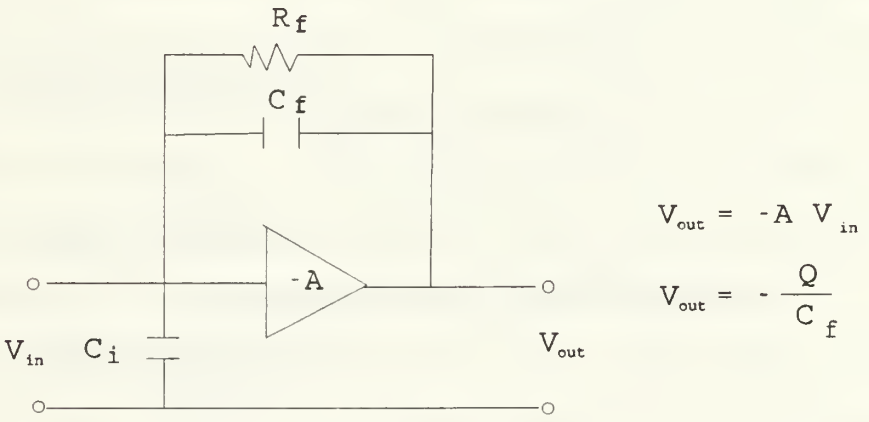

Figure 10. Charge sensitive preamplifier schematic.

3. Amplifier

The amplifier provides both pulse shaping and amplitude gain of the incoming signal pulse. If the amplitude of the incoming signal and gain exceed the output design of the amplifier, a flat top pulse will be observed due to the saturation of the amplifier, Figure 11. Linear amplification will no longer occur at the point of saturation. To overcome the effects of saturation, count rate or gain must be adjusted. Through practical experience, it has been found that reducing the count rate such that the ratio of machine pulses to PHA pulses is in excess of 3:1 will produce a low enough count rate. This simply means reducing the electron beam current of the LINAC to obtain the proper ratio between machine and PHA pulses.

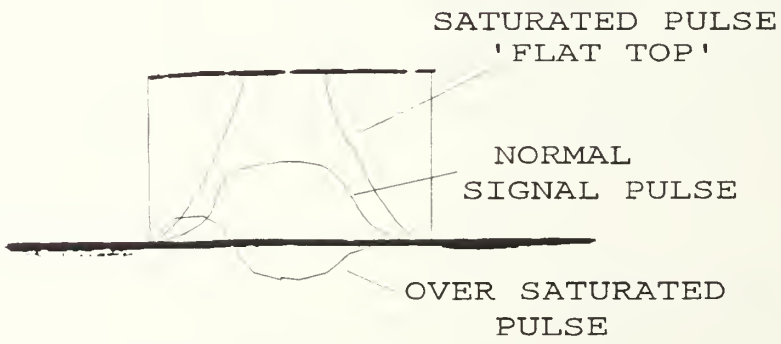

Figure 11. Saturated signal pulse enroute to PHA due to over amplification.

4. Linear Gate

The linear gate, as its name implies, allows signal pulses from the amplifier to pass only when the gate is in the open configuration. Since the gate is closed at all other times signals are blocked from passing through to the pulse height analyzer. The signals that pass through are undisturbed. The linear gate is open and closed by means of a pulse generator. The timing of the pulses to the linear gate will be described in the next section.

Desirable features of the linear gate are low feedthrough in the closed configuration, high linearity and fast switching between the open and closed configurations [Ref. 5].

5. Digital Delay/Pulse Generator

The requirement that the linear gate be opened and closed at a periodic interval is accomplished with the use of a digital delay/pulse generator. The signal to the pulse generator is provided by the master oscillator of the linear accelerator. The master oscillator signals the transmission of a macropulse of electrons to the target chamber.

Through experience, it has been found that delaying the pulse to the linear gate by approximately 20 microseconds after the machine pulse captures the leading edge of the signal pulse. This delay takes into account the difference in time between the master oscillator start signal and the

arrival of the signal pulse at the linear gate. Closing the linear gate at approximately 50 microseconds after opening captures completely the signal pulse.

E. NOISE REDUCTION

Noise can also be reduced by physical means as well as electronic. Sensitive equipment must be protected from RF interference induced by the klystrons and shielding from ground loops will increase the signal to noise ratio and enhance the performance of electronic components.

The x-ray detector was shielded with a copper mesh blanket. The blanket covered the body of the detector protecting the preamplifier from the electomagnetic environment of the end station. In addition, the detector is grounded to reduce the effects of RF interference in processing of the signal pulse.

Since the end station is the primary location of electromagnetic interference, the logical choice is to remove as many of the electronic components in the signal processing chain from this location as possible. The preamp, which is incorporated in the detector itself, must remain in the end station. The bias voltage supply also remains in the end station.

The amplifier, linear gate and pulse generator are all located in the control room, well removed from the EM environment of the end station.

Physically reducing noise by the techniques previously mentioned is often an art form rather than scientific process. Trial and error is usually the norm and patience is a valued virtue.

III. ENERGY CALIBRATION

A. SPECTRUM CALIBRATION

Due to the dynamics of the PXR experiment requiring that x-ray detection and measurement be made while the linear accelerator is operating and the detector is in the end station, a unique problem arises. Electromagnetic noise generated by components of the linear accelerator create interference with the detection of the x-ray emissions of interest. Due to this noise, the energy calibration required will be affected due to the pulse height of the signal of interest being superimposed onto the noise pulse. This will cause a shift in the measured energy of the x-rays compared to energy measurements that might be made in a more benign noise enviroment. An example of the RF noise present during PXR measurements is shown in Figures 12 and 13. These figures are representations of signals going to the pulse height analyzer as seen on an oscilloscope trace. Figure 12 was taken when the klystrons were off and shows little or no deflection in the vertical scale, a sign of no RF noise. Figure 13 shows the same trace after the klystrons have been turned on. A rather obvious change in the pulse height of the signal due to klystron noise is obseved. The requirement for energy

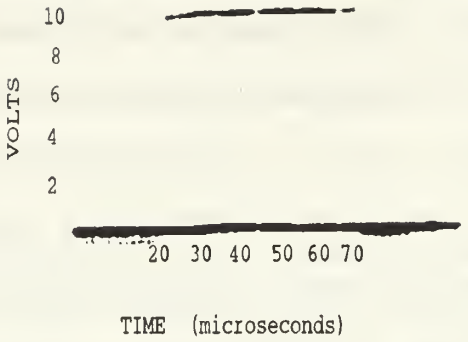

Figure 12. Gated pulse with klystrons off. Horizontal scale is time after machine pulse that linear gate is opened by digital delay pulse generator. The upper trace is the gate signal.

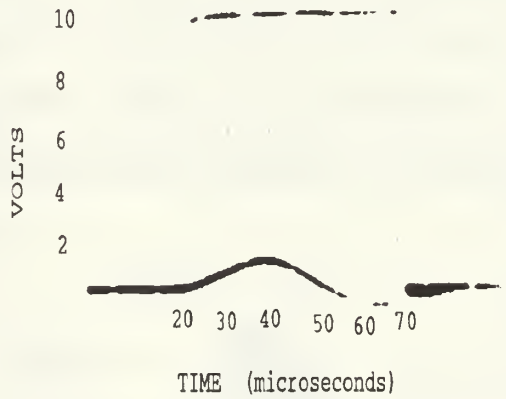

Figure 13. Gated pulse signal with klystrons on. The klystron noise takes on a sinusoidal shape with pulse height interference seen in the vertical scale. The upper trace is the gate signal.

calibrations and noise reduction techniques are needed in order to mitigate the effects of noise interference and achieve consistent and accurate energy measurements.

One technique used in this experiment to reduce the ambient RF noise is to electronically gate the incoming PHA signal so that measurements are made only during the time that x-rays are actually being produced. In specific, signals to the PHA are only permitted to pass during those times that electrons are incident upon the crystal. The timing for the gate is provided by the periodic machine pulse which is fed directly to a pulse generator.

In order to make a thorough examination of energy measurement techniques and provide a source for energy calibration, a target foil consisting of Titanium, Yttrium and Tin were placed on the target ladder, Figure 14. The three foils were arranged in a sandwich configuration such that

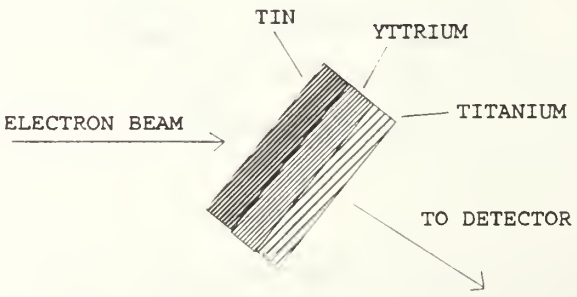

Figure 14. Sandwich foil configuration in target ladder.

energy measurements from the fluorescent x-rays of the three materials could be taken coincidentally. Table II lists the x-ray energies of the target materials used for energy calibration in this experiment.

TABLE II. X-RAY ENERGIES OF TARGET MATERIALS USED FOR ENERGY CALIBRATION.

	K_α (KeV)	K_β (KeV)
TITANIUM	4.51	
COPPER	8.05	8.90
YTTRIUM	14.96	16.74
INDIUM	24.21	27.27
TIN	25.27	28.48

Figure 15 is a typical PHA spectrum taken from the sandwich target foil. The characteristic K shell energy peaks of the three materials can clearly be seen. Additional calibration spectrums using Copper and Indium are illustrated in Figures 16 and 17.

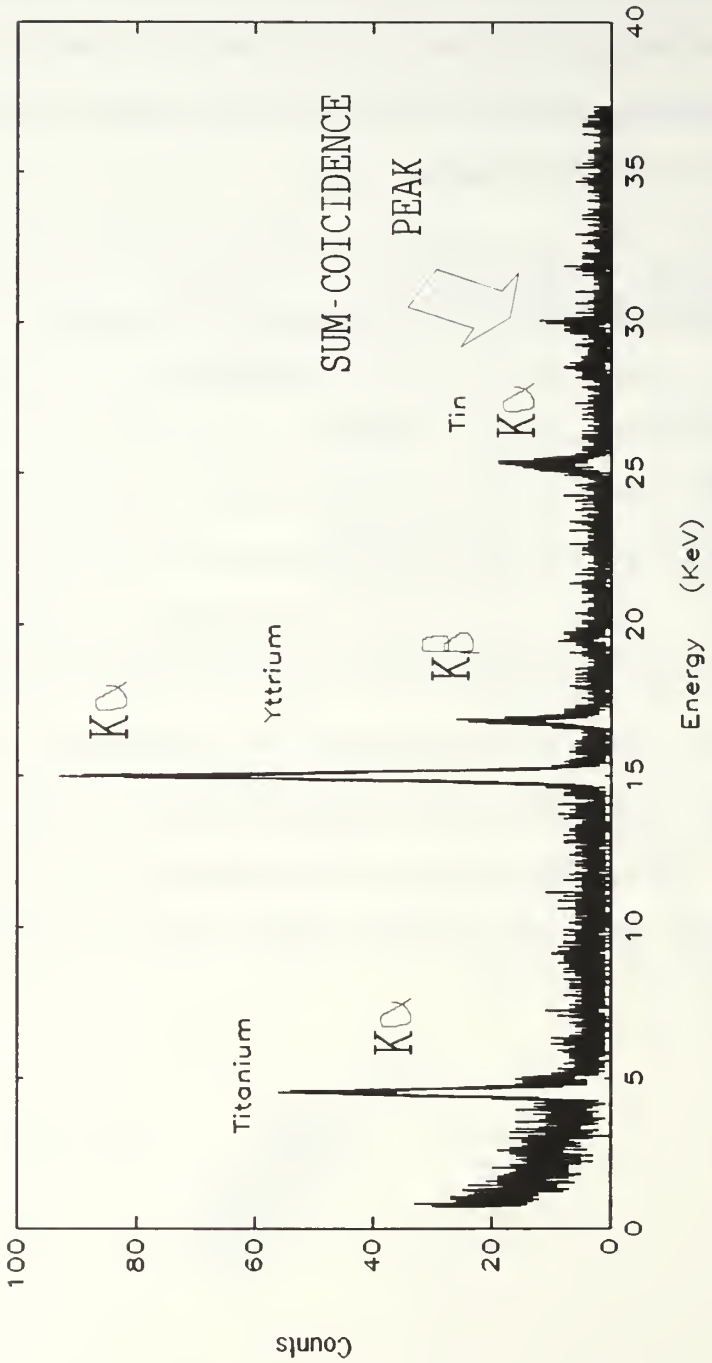

Figure 16. PHA spectrum of sandwich foil used for calibration. Arrow shows a sum-coincidence peak from the K-alpha peak of yttrium.

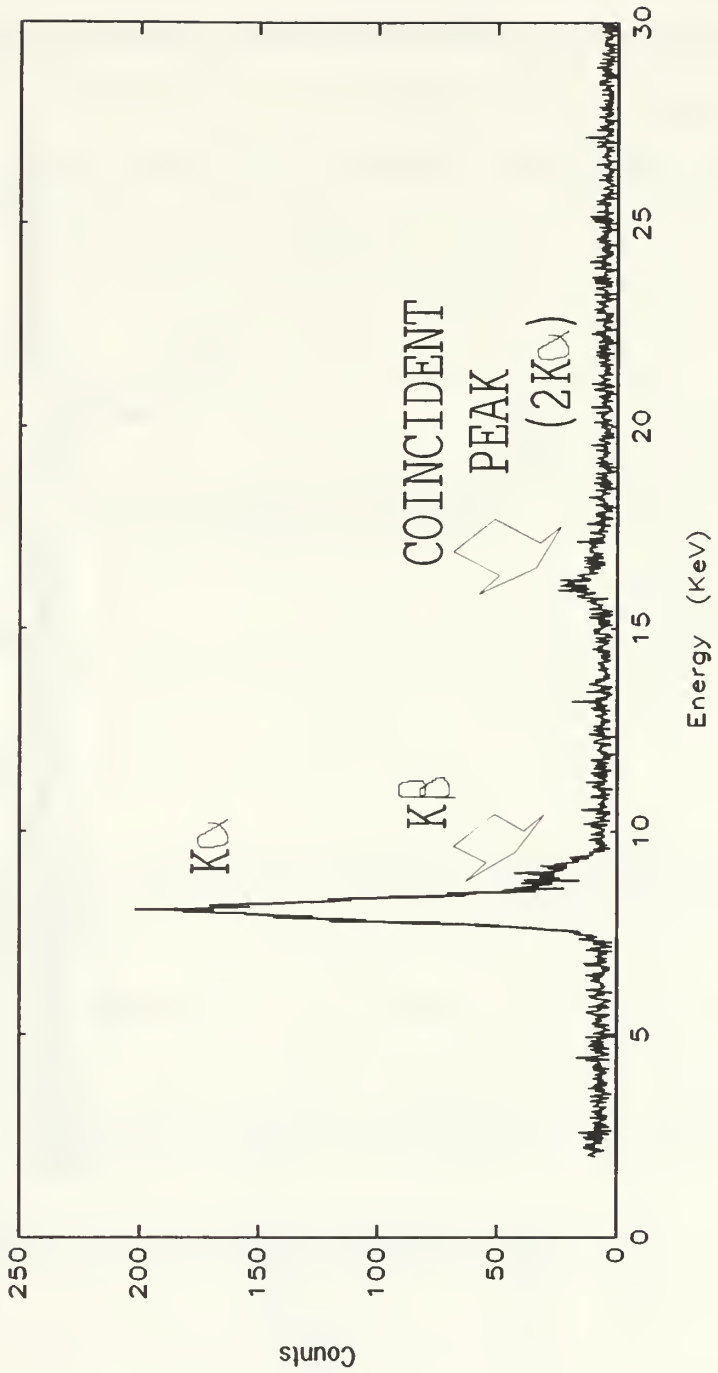

Figure 17. Calibration spectrum using copper as the target material.

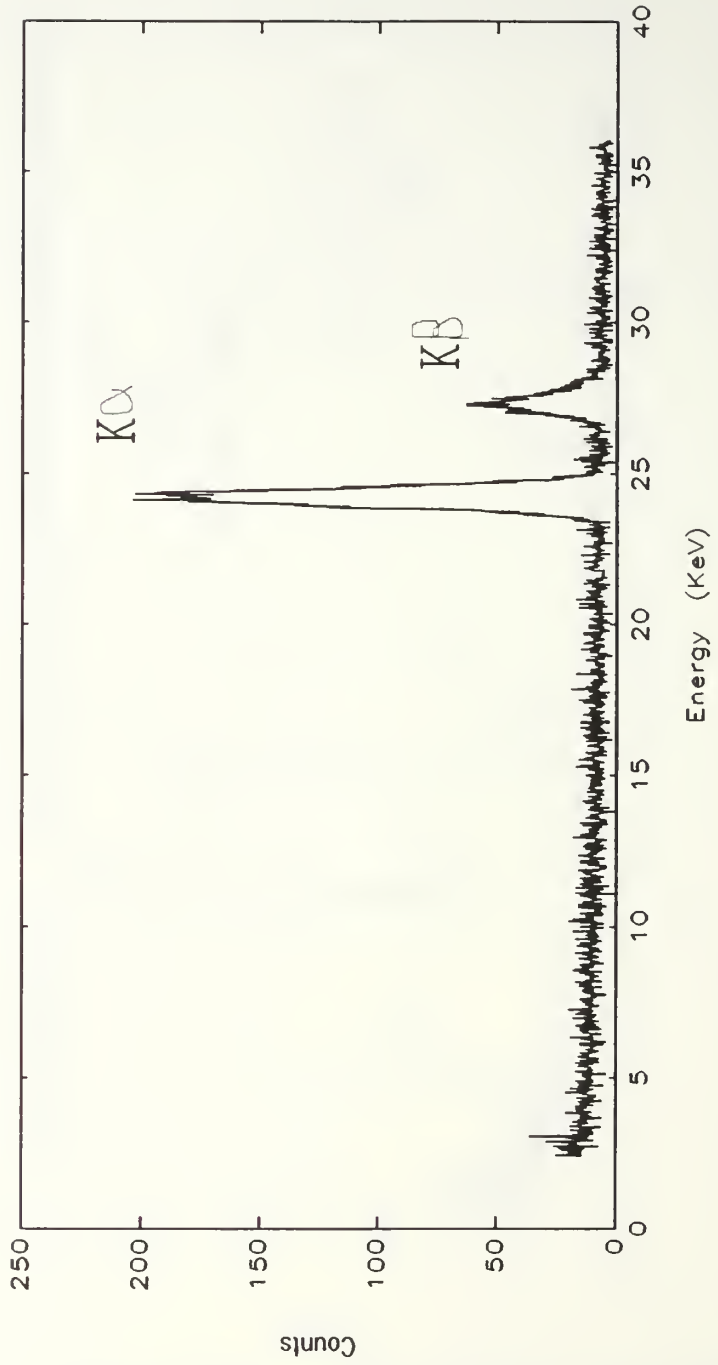

Figure 18. Calibration spectrum using an indium target.

Plotting channel offset versus energy for the same target foil, a shift in energy due to RF noise for a signal that is gated vice one that is not gated can be seen. This is illustrated in Figure 18. Each spectrum equates to approximately 4.7 eV per channel.

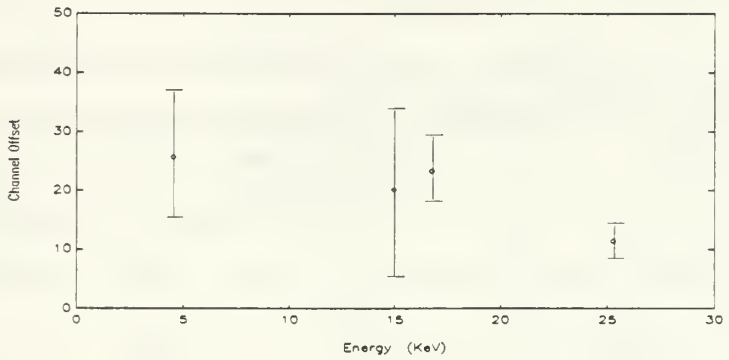

Figure 18. Plot of channel offset of energy centroids between a spectrum taken using gating techniques and one without gating.

Table III summarizes the channel offset between energy peak centroids in both the gated and ungated conditions.

TABLE III. CHANNEL OFFSETS OF ENERGY PEAK CENTROIDS IN BOTH THE GATED AND UNGATED CONDITIONS.

MATERIAL		Channel Offset
Titanium	K_α	25.7±11.1
Yttrium	K_α	20.1±14.2
	K_β	23.3± 5.9
Tin	K_α	11.4± 2.3

The noise reduction introduced by gating the incoming PHA pulse can also be significant. The background noise that is present is supressed and the only noise that is measured is the noise present while the gate is open and the PHA signal pulse is being processed. Table IV summarizes the noise count rate in the regions bounding the signals of interest for the gated and ungated conditions.

TABLE IV. BACKGROUND COUNT RATE IN THE SIGNAL REGIONS OF INTEREST (UNGATED AND GATED).

MATERIAL		counts/sec (Ungated)	counts/sec (Gated)
Titanium	K_α	.477	.218
Yttrium	K_α	.273	.199
	K_β	.160	.057
Tin	K_α	.178	.051

The sandwich foil serves as a calibration source and gating the incoming PHA signal provides a means for noise reduction, all necessary in obtaining accurate energy measurements. For total consistency throughout a data collection set, the gating parameters must also remain constant. The time after the machine pulse at which the gate is open and the width of the gate can not be changed at any time during which PXR data is being collected or a new energy calibration will be necessary. Table V is channel offset between energy centroid data for two different gated runs

whose only difference was the time at which the gate was open. The width of the gate, 50 microseconds, was the same for both runs.

TABLE V. CHANNEL OFFSET BETWEEN ENERGY CENTROIDS FOR GATED DATA WITH INITIAL GATE PULSE DIFFERING IN DELAY BY 10 MICROSECONDS.

MATERIAL	Channel Offset
Titanium K_α	20.6±41.3
Yttrium K_α	15.2±56.1
Tin K_α	-4.1±5.9

B. EXPERIMENTAL PROCEDURE

The sandwich foil used in these experiments, titanium, yttrium and tin, provided a means of calibration throughout the energy spectrum of interest. The corresponding characteristic energies of these materials is approximately 5 KeV, 15 KeV,and 25 KeV respectively, which covers the maximum detection efficiency region of the Si(Li) detector.

The calibration of the spectra themselves were performed using the calibration algorithm provided in the Nucleus Pulse Height Analysis program. A sufficient number of counts in the peak, preferably greater than fifty, should be collected to provide data for the calculation of the centroid within the region of interest surrounding the peak.

An additional consideration, spectrum drift, should also be accounted for with PXR data collection periods which are in

excesss of several hours. Taking periodic calibrations separated by several hours have shown consistent drifts in the spectrum. These drifts have been observed with the linear accelerator operational as well as with the accelerator shut down. Figure 19 shows the drift using Fe55 and Cs137 sources over a period of several days. This points to an energy drift being induced somewhere within the energy signal processing chain; detector, preamplifier, amplifier or possibly the bias voltage supply. Although the drift is observed, individual spectra preserve the linearity property. The net effect is a slow increase in the overall gain of the signal processing system.

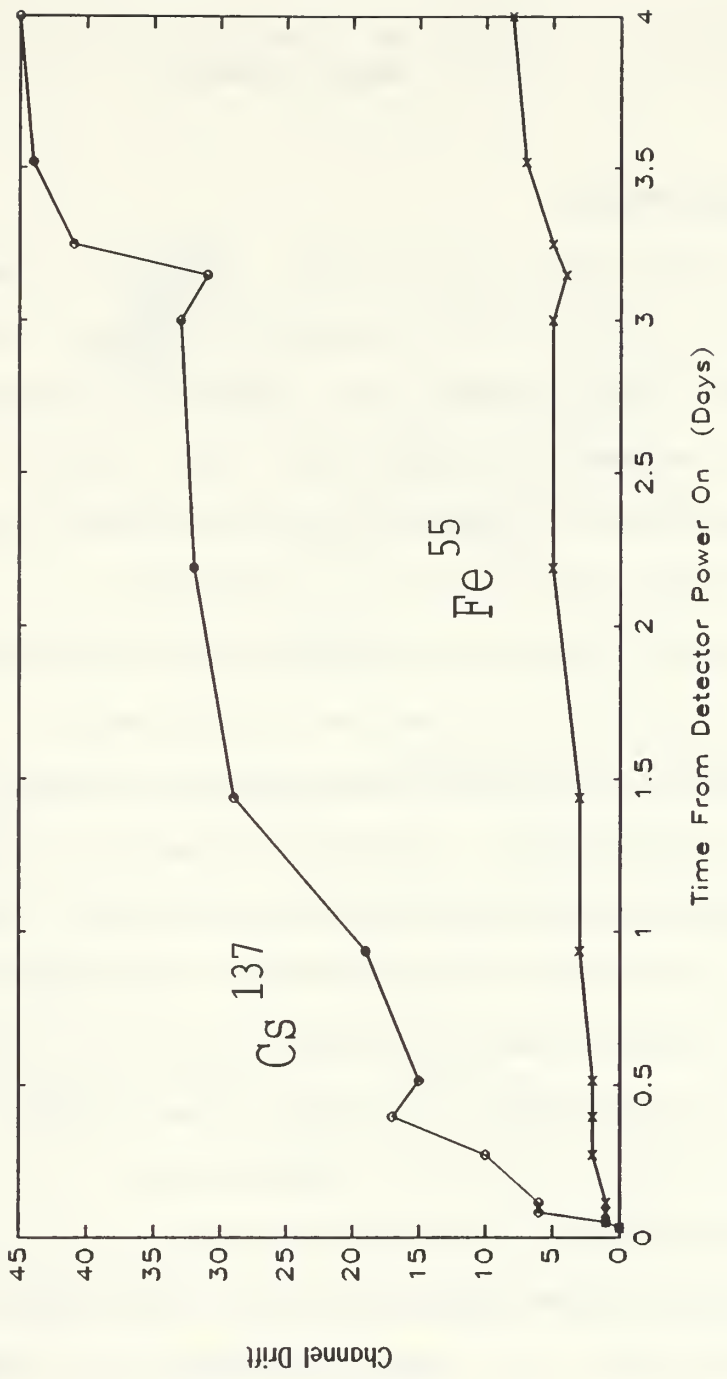

Figure 19. Energy drift as a function of time. The linearity property is maintained at each data collection point.

IV. BEAM INTENSITY

A. INTRODUCTION

When PXR data is collected, the total number of x-rays produced at a particular energy are recorded. This data yields a relative flux or the total number of photons created. In order to compare the PXR data with theory, the number of photons produced for every electron incident upon the crystal, or absolute flux, must be calculated. It is therefore necessary to determine the total number of electrons incident on the crystal for a given set of PXR data.

Similar to the energy calibration procedures described in the previous chapter, a sandwich target foil can again be used in determining the electron beam current. Using the known physical and radiative properties of the target materials and with an accurate measurement of the total number of K shell radiative transitions, the total number of electrons incident upon the target foils can be determined.

Collecting data from the three target foils simultaneously and calculating the current from the individual foils, a check for consistency in the calculation of beam current is provided. Attenuation of the the x-rays of various energies and the geometry of the photon paths must be accounted for.

Figure 20 illustrates the target foil in the end chamber and the materials which attenuate the x-rays in transit to the detector.

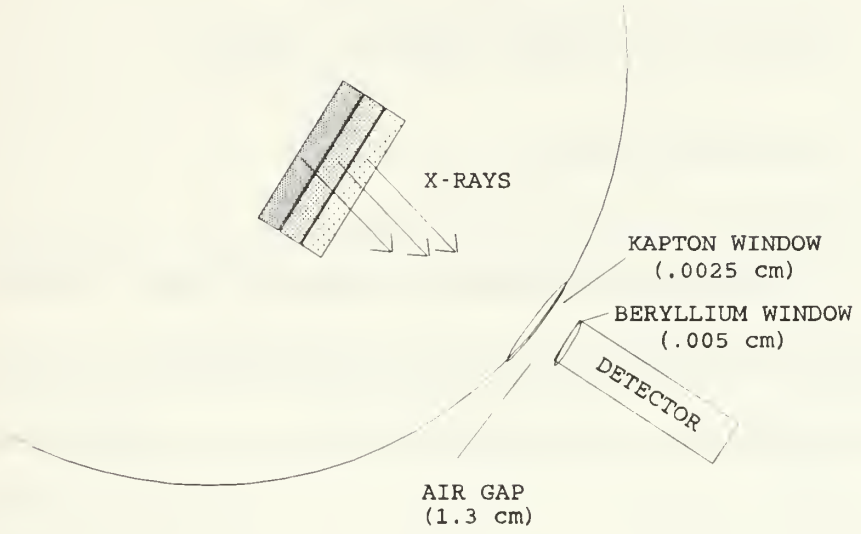

Figure 20. Target ladder configuration and attenuating materials.

The total number of electrons incident upon the target foils is determined by equation 2.

$$N_e = \frac{(N_{ph})\,(AW)}{(\sigma)\,(\frac{\Omega_d}{4\pi})\,(\rho)\,(N_o)\,(f_{dex})\,(t_{eff})\,(a)\,(\epsilon)} \qquad (2)$$

N_c - Total number of electrons incident on target

N_{ph} - Number of photons detected

AW - Atomic weight of target foil (g/mole)

σ - Electron interaction cross section (cm^2)

Ω_d - solid angle subtended by detector (sr)

ρ - density of target materwl (g/cm^3)

N_o - Avagadro's Number ($6.02x10^{23}$)

f_{dex} - radiative transition probability

t_{eff} - effective thickness of target (cm)

a - total attenuation factor of photons

ϵ - Detector relative efficiency

B. EXPERIMENTAL PROCEDURE

The objective of the procedures used in this experiment was to check for self consistency in the calculation of total electrons incident upon the target material. Again using the sandwich foil three calculations of beam intensity could be calculated and compared.

The target foils were arranged in the target ladder and the ladder was rotated 60 degrees counterclockwise to the beam line. The target chamber configuration is depicted in Figure 21.

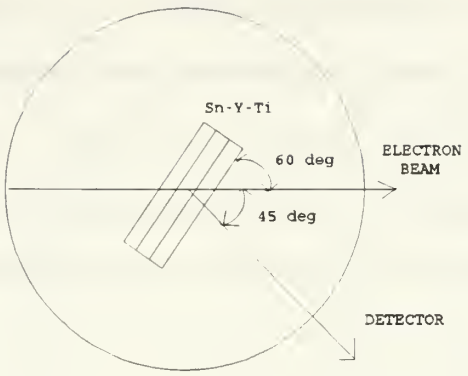

Figure 21. Sandwich foil configuration in the target chamber used in calculating beam intensity.

The thickness of each foil was determined by measuring the area and mass of the individual foils and calculating the thickness using the known denity of Titanium, Yttrium and Tin.

The effective thickness of each target is a function of the geometry between the target ladder and the detector. In all cases in this experiment the effective thickness of each target was determined by correcting the normal thickness by $\cos(30^\circ)$.

Attenuation was determined using characteristic photon energies and obtaining attenuation coefficients [Ref.8]. The total attenuation of the characteristic photons, $e^{\Sigma(-\mu\rho t)}$, was then calculated. Photon production was assumed to be generated half way through the target material. Results from these calculations are listed in Tables VI and VII.

Efficiency of the detector at the various incident x-ray energies must also be accounted for in calculating the beam

intensity. The efficiency of the Si(Li) detector is a function of energy. For very soft x-rays attenuation is due to the beryllium entrance window. At higher energies the detector becomes transparent to photons, capturing only a small part of the photon energy [Ref. 6]. The efficiency curves are shown in Figure 22.

TABLE VI. PROPERTIES OF TARGET MATERIALS.

MATERIAL	NORMAL THICKNESS (cm)	ATTENUATION COEFFICIENT(cm-2/g)
Tin	2.75×10^{-3}	1.09e+3 (4.5 Kev) 4.70e+1 (14.9 Kev) 1.14e+1 (25.3 Kev)
Yttrium	6.03×10^{-3}	5.79e+2 (4.50 Kev) 2.30e+1 (14.9 Kev) 3.70e+1 (25.3 Kev)
Titanium	1.64×10^{-3}	1.09e+2 (4.50 Kev) 3.62e+1 (14.9 Kev) 8.12e+0 (25.3 Kev)
Air	1.3e-2	5.47e+1 (4.50 Kev) 1.63e+0 (14.9 Kev) 4.74e-1 (25.3 Kev)
Beryllium	5.0×10^{-3}	5.99e+0 (4.50 Kev) 3.08e-1 (14.9 Kev) 1.93e-1 (25.3 Kev)
Kapton	2.5×10^{-4}	3.49e+1 (4.50 Kev) 1.05e+0 (14.9 Kev) 3.60e-1 (25.3 Kev)

TABLE VII. ATTENUATION FACTORS OF PHOTONS THROUGH TARGET MATERIALS($e^{(-\mu\rho t)}$).

ENERGY (Kev)/ MATERIAL	25.3 Kev Sn	14.9 Kev Y	4.50 Kev Ti
Tin	.888	-	-
Yttrium	.356	.725	-
Titanium	.939	.757	.657
Air	.999	.997	.912
Beryllium	.998	.997	.947
Kapton	.999	.996	.883
TOTAL	**.296**	**.543**	**.501**

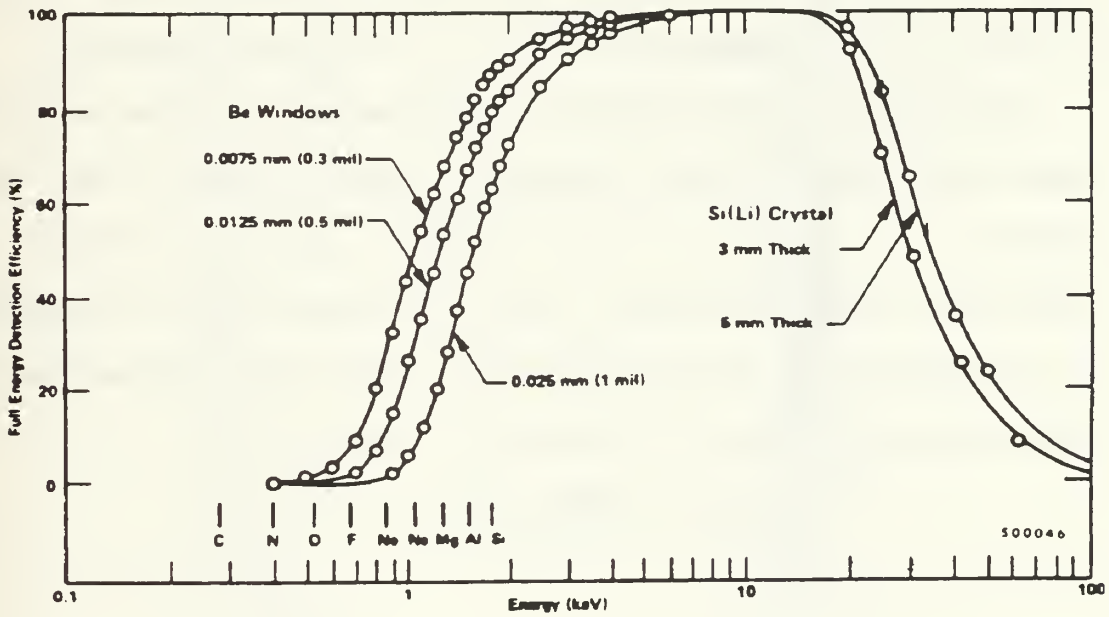

Figure 22. Efficiency curves for Si(Li) detector.

Using the data derived from the spectrum in Figures 23-25 the total number of counts under each peak could be determined. The photon count data can now be converted into the total number of electrons incident upon the target foil.

Electron interaction cross sections [Ref. 9] and radiative transition probabilities [Ref. 10] are obtained using an incident electron energy of 85 MeV.

Two different Si(Li) detectors were used in the course of these experiments, a Canberra and ORTEC detector. The solid angles subtended by the detectors are listed in Table VIII. as well as all other properties of the target materials.

Using the values listed in Table VIII, three separate spectrums were collected using the sandwich foil. The total number of electrons , N_e, incident upon the foils was calculated using equation 2. based upon the number of photons, N_{ph}, counted under each energy peak. The results using the two detectors are listed in Tables IX, X and XI.

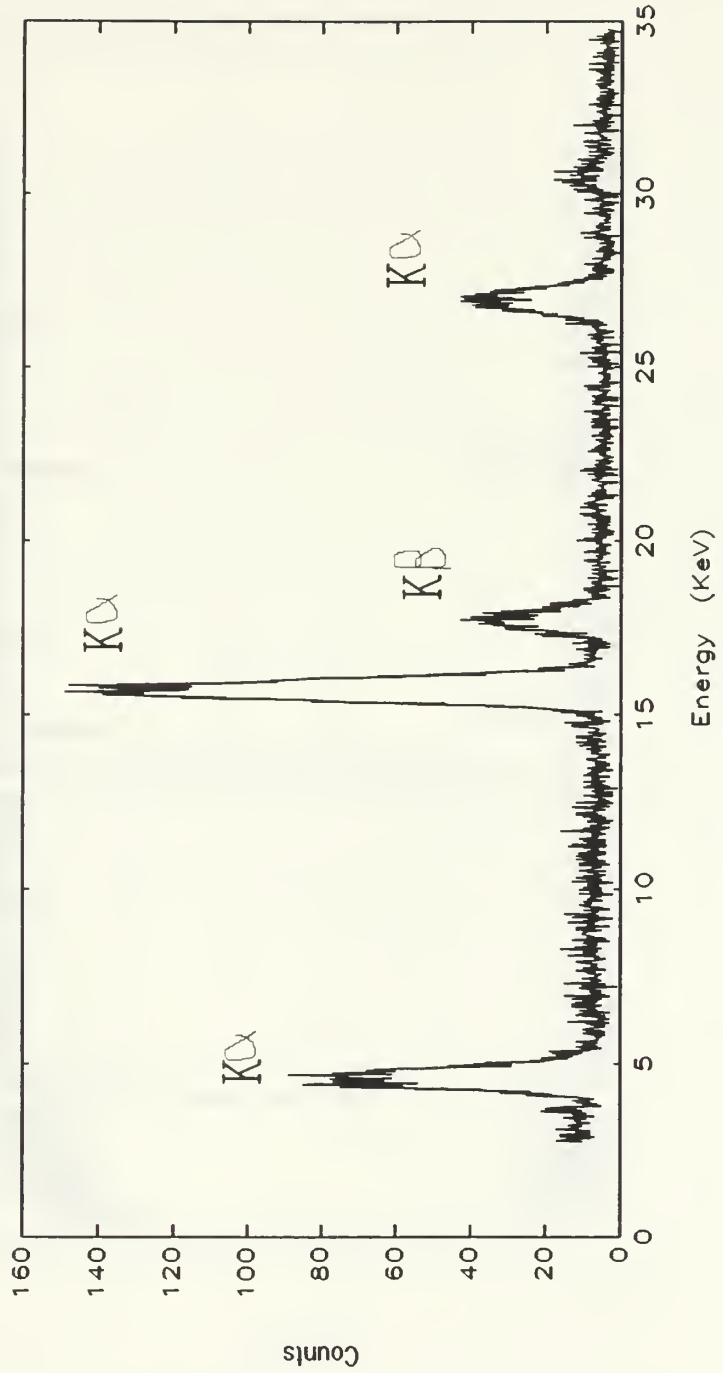

Figure 23. PHA spectrum of sandwich foil using ORTEC detector. Corresponding data is listed in Table VIII.

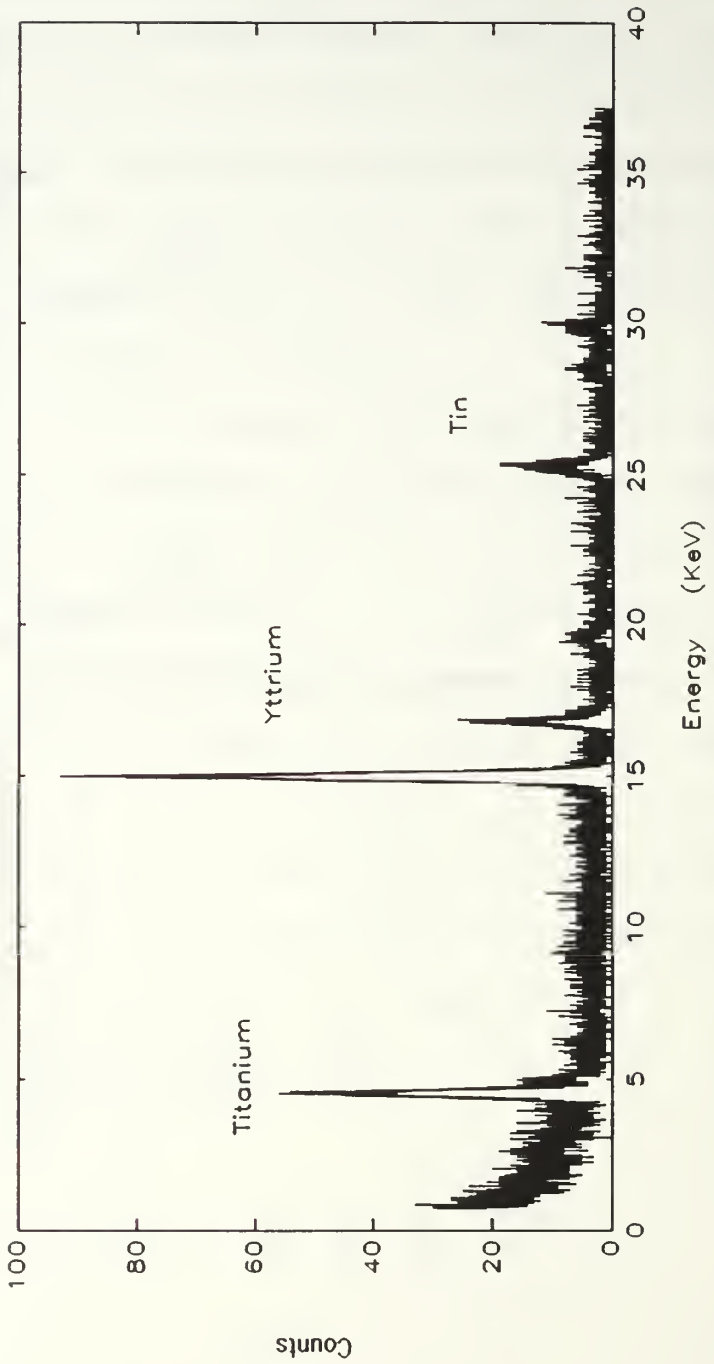

Figure 24. PHA spectrum of sandwich foil using Canberra detector. Corresponding data is listed in Table X.

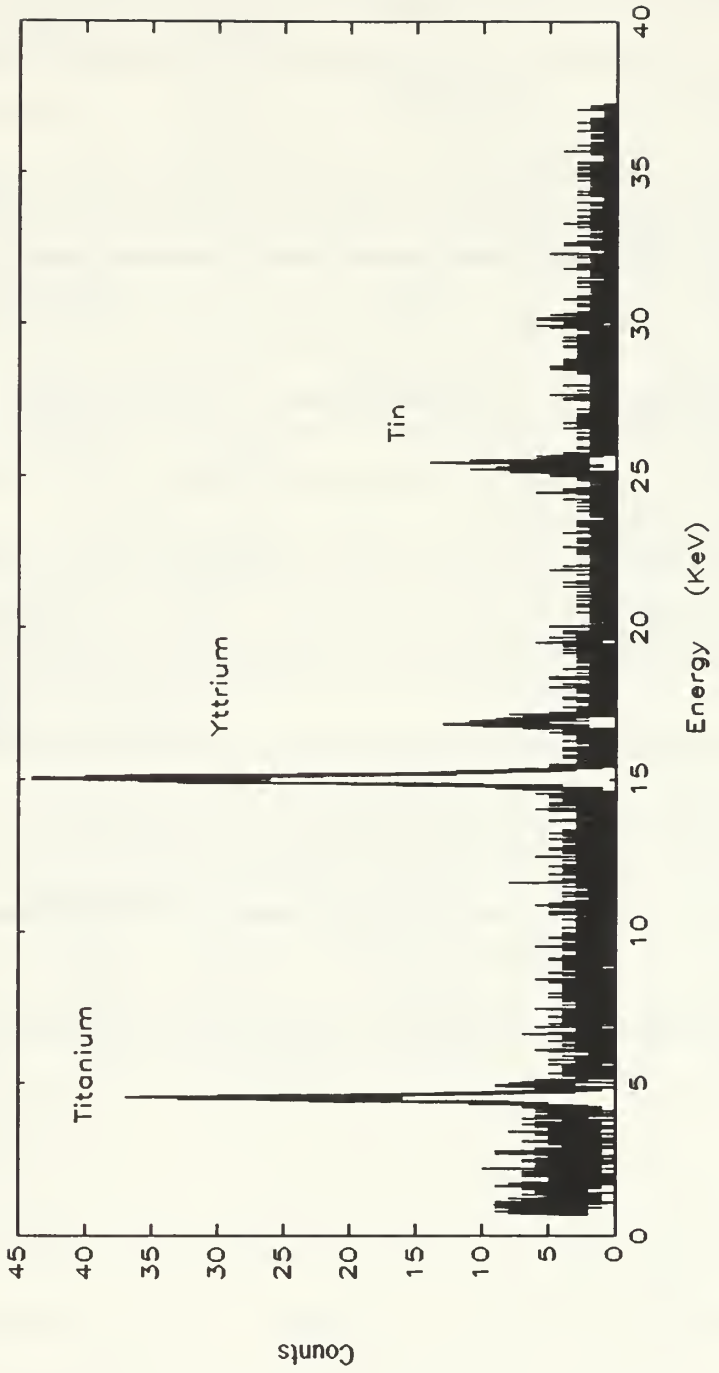

Figure 25. PHA spectrum from sandwich foil using Canberra detector. Corresponding data is listed in Table XI.

TABLE VIII. TARGET MATERIAL PROPERTIES USED TO CALCULATE BEAM INTENSITY.

TARGET / VALUE	TIN	YTTRIUM	TITANIUM
AW (g/mole)	118.69	88.91	47.9
σ (barns) (85 MeV)	$1.02X10^2$	$2.0X10^2$	$7.0X10^2$
Detector Window Area (mm^2)	201.1 (Canberra and ORTEC)		
Target/Detector Separation (mm)	279.4 (Canberra) 977.9 (ORTEC)		
Ω_d (sr)	$2.58x10^{-3}$ (Canberra) $2.10x10^{-4}$ (ORTEC)		
ρ (g/cm^3)	7.31	4.47	4.54
f_{dex}	.712	.602	.192
t (cm)	$2.75x10^{-3}$	$6.03x10^{-3}$	$1.64x10^{-3}$
a	.296	.543	.501
ϵ	.9	.95	.95

TABLE IX. CALCULATION OF BEAM CURRENT USING ORTEC DETECTOR. RATIO OF MACHINE PULSES TO PHA PULSES IS 3:1. RUN TIME IS 7261 SECONDS.

	TIN	YTTRIUM	TITANIUM
N_{ph}	1282±204	4370±161	1996±212
N_e ($x10^{10}$)	3.37±1.18	1.99±.64	1.72±.57
Average Current (amps) $x10^{-13}$	7.47±2.61	4.41±1.41	3.81±1.26

TABLE X. CALCULATION OF BEAM CURRENT USING CANBERRA DETECTOR. RATIO OF MACHINE PULSES TO PHA PULSES IS 2:1. RUN TIME IS 5572 SECONDS.

	TIN	YTTRIUM	TITANIUM
N_{ph}	1506±255	7749±236	3437±364
N_e ($x10^{9}$)	3.22±1.16	2.89±.9	2.43±.8
Average Current (amps) $x10^{-14}$	9.30±3.35	8.35±2.59	7.02±2.32

TABLE XI. CALCULATION OF BEAM CURRENT USING CANBERRA DETECTOR. RATIO OF MACHINE PULSES TO PHA PULSES IS 7:1. RUN TIME IS 4212 SECONDS.

	TIN	YTTRIUM	TITANIUM
N_{ph}	453±95	2553±194	1214±177
N_e ($x10^{8}$)	9.67±3.67	9.48±3.13	8.57±2.99
Average Current (amps) $x10^{-14}$	3.70±1.41	3.62±1.19	3.28±1.15

Electron-interaction cross sections listed are accurate to within 30 percent [Ref. 9]. Radiative transition probabilities are accurate to within 10 percent [Ref. 10].

The results shown in Table XI yield the most consistent results, within 5 percent of the average. This is in part due

to the fact that the current is smallest on this run compared to the others, therefore the count rate for each characteristic peak was smaller. Since coincident counting is proportional to the square of the count rate (equation 1), the number of sum-coincident peaks would be proportionally less. This corresponds to less information being lost in the primary peaks and therefore better counting statistics. The important conclusion to be drawn is that the lower the current the LINAC is operated at, the less the degrading effects in the energy peaks of interest due to sum-coincidence effects. As current is increased, possibly in an attempt to obtain data more quickly, the sum-coincidence effect must be taken into account for accurate analysis.

V. CONCLUSIONS

Parametric x-ray radiation experiments require that x-ray detection and measurement be done in an elecromagnetic noise enviroment. Due to this constraint, energy calibrations by conventional methods, i.e. sources, is not possible. The method outlined in this paper of using target foils as both a calibration source and beam intensity source for PXR spectrum analysis has proved very successful and accurate.

A target foil can be placed on the back of a crystal and energy calibration data can be collected in conjunction with PXR data. This allows for simultaneous collection of PXR, energy calibration and beam intensity information. By bonding a thin strip of tin to the back of a carbon graphite crystal used for parametric x-ray radiation production, a self contained energy calibration source and LINAC beam intensity scale are provided. A sample PXR spectrum along with the Tin calibration peak is shown in Figure 26 [Ref. 9].

Characteristics and effects of solid state detectors must also be considered when collecting data inorder to make an accurate analysis. As electron beam current is increased, the count rate of x-ray production increases. As a result, the degrading effects of sum-coincidence counting are also increased. In experiments such as PXR, energy peaks are

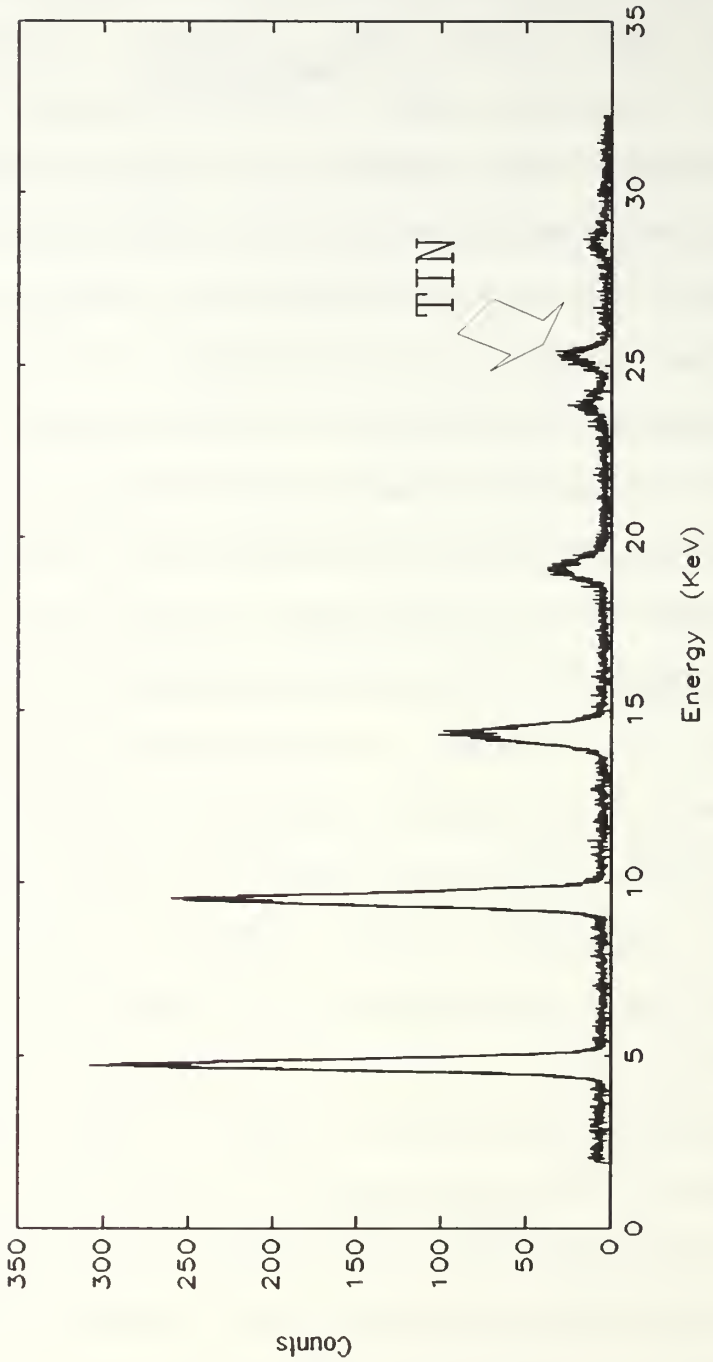

Figure 26. PXR spectrum of carbon graphite. Tin is used as a calibration source. PXR and calibration data are collected simultaneously.

integer multiples of one another and sum-coincidence effects are not readily apparent by observing the spectrum. To decrease these effects, beam current should be as low as possible.

The methods described of energy calibration and beam intensity calculation will allow for a more complete, accurate and thorough examination of PXR data.

LIST OF REFERENCES

1. U.S. Department of Energy Project Summary, Parametric Radiation as an Intense Monochromatic X-ray Source, by M. A. Piestrup, 4 February 1992.

2. DiNova, K., Enhanced Higher Order PXR Production, Master's Thesis, Naval Postgraduate School, Monterey, California, December 1992.

3. Carlson, B. A., and Gisser, D. G., Electrical Engineering, Addison-Wesley, 1981.

4. Michael, S., "Semiconductor Physics", class notes handout, 1991.

5. Knoll, G. F., Radiation Detection and Measurement, John Wiley and Sons, 1979.

6. Canberra Industries, Si(Li) Detector System Instruction Manual, 1991.

7. Evans,R. D., The Atomic Nucleus, M^{c}Graw-Hill, 1955.

8. Hubbel, J. H., XCOM: Photon Cross Sections On A Computer, U.S. Department of Commerce, NBSIR 87-3597, 1991.

9. Perkins, S. T., Tables and Graphs of Electron-Interaction Cross Sections from 10 eV 100 GeV, Lawrence Livermore National Laboratory, UCRL-50400 Vol. 31, 1991.

10. Perkins, S. T., Tables and Graphs of Atomic Subshell and Relaxation Data, Lawrence Livermore National Laboratory, UCRL 50400 Vol.30, 1991.

INITIAL DISTRIBUTION LIST

1.	Defense Technical Information Center Cameron Station Alexandria, Virginia 22304-6145	2
2.	Library, Code 0142 Naval Postgraduate School Monterey, California 93943-5002	2
3.	Dr. K.E. Woehler Department of Physics Naval Postgraduate School Monterey, California 93943-5002	1
4.	Professor X.K. Maruyama Department of Physics Naval Postgraduate School Monterey, California 93943-5002	2
5.	Dr. M.A. Piestrup Adelphi Technology, Inc. 2181 Park Boulevard Palo Alto, California 94306	1
6.	Dr. D.W. Rule, Code R41 Naval Surface Weapons Center Silver Spring, Maryland 20903-5000	1
7.	Dr. R.B. Fiorito, Code R41 Naval Surface Weapons Center Silver Spring, Maryland 20903-5000	1
8.	Dr. J. Scofield Lawrence Livermore National Laboratory University of California Livermore, California 94551	1
9.	Dr. J.H. Hubbell Center for Radiation Research National Bureau of Standards Gaithersburg, Maryland 20899	1

10. Mr. D. Snyder, Code 61Ph 1
Department of Physics
Naval Postgraduate School
Monterey, California 93943-5002

11. LT. T.J. Fasanello 2
8592-A SW. 91st St.
Ocala, Fl. 34481